Applied Surface Science 574 (2022) 151339

Contents lists available at ScienceDirect

Applied Surface Science

journal homepage: www.elsevier.com/locate/apsusc

Full Length Article

Laser-Induced fluorinated graphene for superhydrophobic surfaces with anisotropic wetting and switchable adhesion

Ki-Ho Nam [a,b], Moataz Abdulhafez [a], Golnaz Najaf Tomaraei [a], Mostafa Bedewy [a,c,d,*]

[a] Department of Industrial Engineering, University of Pittsburgh, 3700 O'Hara Street, Pittsburgh, PA 15261, USA
[b] Department of Textile System Engineering, Kyungpook National University, Daegu 41566, Republic of Korea
[c] Department of Chemical and Petroleum Engineering, University of Pittsburgh, 3700 O'Hara Street, Pittsburgh, PA 15261, USA
[d] Department of Mechanical Engineering and Materials Science, University of Pittsburgh, 3700 O'Hara Street, Pittsburgh, PA 15261, USA

ARTICLE INFO

Keywords:
Laser-induced graphene
Nanocarbons
Micropatterning
Fluorinated polyimide
Heteroatom self-doping
Anisotropic wettability
Superhydrophobic surface
Parahydrophobicity
Droplet adhesion

ABSTRACT

We present a facile direct-write approach for patterning fluorine-doped nanocarbons directly on molecularly engineered polymers for superhydrophobic and parahydrophobic surfaces. We first synthesized two different polymer films, non-fluorinated and fluorinated polyimides (PIs), by two-step procedure to create poly(amic acid) precursors, followed by thermal curing. Morphology and chemical composition were controlled by adjusting the programmed scan line pitch from 101.6 to 508 μm during lasing to achieve superhydrophobicity with a water contact angle (CA) up to 156° in the direction perpendicular to carbonized lines. Droplets exhibited strong adhesion on our porous graphene micropatterns even when held at vertical and inverted orientations, indicating a Cassie impregnating state of wetting. Parahydrophobic F-LINC with line pitch of 355.6 μm exhibits high dynamic CAs along both perpendicular ($\theta_{A\perp} = 165°$, $\theta_{R\perp} = 127°$) and parallel directions ($\theta_{A\parallel} = 147°$, $\theta_{R\parallel} = 87°$) as well as highly anisotropic CA hysteresis ($\Delta\theta_{\perp} = 38°$, $\Delta\theta_{\parallel} = 60°$). Moreover, we demonstrate strain-induced switchable adhesion by leveraging substrate curvature control. Further, we show that our micropatterned polymer films can be used for transferring droplets without any loss or contamination. Hence, our approach offers new insights into designing interfaces for droplet manipulation, pick-and-place applications, and localized control of reactions.

1. Introduction

Engineered surfaces with tunable wettability have emerged in recent years, owing to their broad technological implications in the field of environment, energy, and health [1-3]. Inspired by nature, superhydrophobic surfaces with an apparent water contact angle (CA) larger than 150° have been developed by mimicking the behavior of functional interfaces found in various plants and animals [4-6]. One of the well-known biological model systems of superhydrophobic surfaces is the rose petal, which has strong adhesion to water, i.e. water droplets cannot move at any tilted angles on the surface while maintaining a high CA [7]. This behavior, referred to as parahydrophobicity, [8] is ideal for water collection, microdroplet transportation, ultrafiltration, and reverse osmosis applications [9-11]. Tailoring the adhesive properties on superhydrophobic surfaces requires a delicate balance between surface chemistry and hierarchical topography [12]. Engineered superhydrophobic surfaces have been fabricated by various lithographic techniques: photolithography, [13,14] reactive ion etching, [15] capillary lithography, [16,17] micro-molding and others [18]. Nevertheless, many of these techniques are not suitable for flexible substrates, and are generally both complex and costly. Hence, new scalable methods for fabricating superhydrophobic surfaces with controllable adhesion directly on polymers are needed.

Graphene is an ideal candidate for functional superhydrophobic surfaces not only due to the non-polar carbon structure itself but also due to its large specific surface area, tunable surface roughness, low density, and abrasion resistance [19]. Much effort has been devoted to the biomimetic artificial fabrication of water-repellent surfaces printed and patterned with graphene. By tuning its surface wetting properties, graphene surfaces can be used in the production of aerogels, [20] heaters, [21] and gas sensors [22]. However, many of the manufacturing methods for generating these nanotextured graphene surfaces rely on mask-based patterning [22] or paste-based 3D printing, [20] which are complex multi-step indirect processes, or are time-consuming and

* Corresponding author at: Department of Industrial Engineering, University of Pittsburgh, 3700 O'Hara Street, Pittsburgh, PA 15261, USA.
E-mail address: mbedewy@pitt.edu (M. Bedewy).

https://doi.org/10.1016/j.apsusc.2021.151339
Received 10 April 2021; Received in revised form 16 September 2021; Accepted 17 September 2021
Available online 27 September 2021

expensive. In contrast, direct laser processing does not require pre-designed and mask fabrication (to be followed by pattern transfer), and does not require preparation of printable paste.

Indeed, Direct laser writing has recently been shown to uniquely enable tuning the nano/micro-scale structures on a variety of surfaces such as wood, [23] paper, [24,25] cork, [26] glass, [27] and engineering plastics. [28,29] It is a fast and scalable approach to generate functional surface structures, typically in atmospheric conditions without the need for low vacuum conditions, or harsh chemical environments. Moreover, the direct-write nature of laser-based approaches enable a great flexibility in pattern design, as it eliminates the need for costly masks. In particular, laser-induced graphene (LIG) formation by local carbonization of polyimide (PI) is a powerful technique for creating patterns of high surface area three-dimensional graphene. [28,30-32] Hence, it is an ideal candidate for scalable manufacturing of flexible surfaces with tunable wetting behavior. [33-36] Various hierarchical morphologies ranging from porous to fibrous and complex 3D structures can be spatially controlled by modulating the lasing parameters such as laser power, raster speed, beam defocus, and pulsing density. [30,31,34] Also, adjusting the oxygen content in different gas atmospheres during lasing was found to control the wetting properties of LIG on commercial PI (Kapton®) achieving both superhydrophilic and superhydrophobic surfaces.[37] Additionally, F-doping of the LIG surface was demonstrated under sulfur hexafluoride (SF_6) gas atmosphere, where an even higher CA above 160° could be reached due to the low surface energy of the C—F bonds.[37] However, gas atmosphere control complicates LIG manufacturing and necessitates the use of complex environmental chambers that limit scalability and increase the negative environmental impact of the process if toxic gases are used/released. Alternatively, antiwettingsurfaces were fabricated from LIG by impregnating the porous graphene with hydrophobic polymers, [38] which also complicates the fabrication process and may render it less sustainable. On the other hand, creating engineered LIG micropatterns in atmospheric conditions to tune hydrophobicity, [34-36] is most promising for single-step scalable and green manufacturing of superhydrophobic wetting on polyimide.

Importantly, all the above-mentioned reports on LIG for tailoring surface superhydrophobicity relied on commercial PI films (e.g. Kapton®), which limits the ability to control the surface chemistry and atomic structure of the produced graphene material. Thus, a facile strategy to precisely modulate both LIG chemical functionalization and hierarchical morphology based on molecular control of PI is needed for manufacturing artificial superhydrophobic surfaces with controllable adhesion. Herein, we show a process for directly creating superhydrophobic graphene-based micropatterned surfaces from fluorinated PI as the newly designed precursor for localized laser carbonization. Lasing fluorinated PI uniquely enables the efficient photothermal F-doping and produces desirable nano/micro-scale hierarchical porous structures, which are critical for tuning antiwetting and adhesion. Moreover, combined with directional patterning of parallel periodic lines, anisotropic wetting properties are also demonstrated. In our approach, both the geometry and hierarchical morphology of carbonized structures are tailored by spatial modulation of laser scanning to leverage proximity effect and create desired profiles of cumulative laser fluence. We systematically investigated the anisotropic wetting behavior along the directions parallel and perpendicular to line patterns. Our F-doped graphene micropatterning approach created well-ordered hierarchical surfaces that remained superhydrophobic but were found to be strongly adhesive to water droplets. Further, we demonstrate the use of our engineered surfaces for transport of water droplets without any loss or contamination by utilizing curvature-driven switching of droplet adhesion, which is promising for various applications including anti-biofouling, [39,40] air-filtration, [41] water-treatment membranes, [42] fuel cells, [43] and energy storage. [44] In particular, our proposed droplet manipulation and pick-and-place strategies are promising for integration with microfluidics systems, [34] lab-on-a-chip devices, [45] and point-of-care diagnostics [46].

2. Experimental section

2.1. Materials

Pyromellitic dianhydride (PMDA), 4,4′-(hexafluoroisopropylidene) diphthalic anhydride (6FDA), and 2,2′-bis(trifluoromethyl)benzidine (TFMB)were purchased from Tokyo Chemical Industry, Co., Ltd. (Japan). 1-Methyl-2-pyrrolidinone (NMP) was purchased from Sigma-Aldrich (USA). All chemicals were used without further purification.

2.2. Polyaddition, Imidization, and film preparation

The synthesis routes of PIs are given in Fig. 1(a). The detailed procedure is as follows: The polymerization was carried out by reaction of equimolar amounts of TFMB diamine with 6FDA tetracarboxylic dianhydride at a concentration of 16 wt% solid in anhydrous NMP. Polycondensation was performed at 23 °C for 24 h and yielded viscous poly (amic acid) (PAA) intermediate solution. The PAA solution was coated onto a clean glass substrate using a high precision adjustable film coating applicator with a blade gap of 1000 μm. The PAA was subsequently converted into PI film via cyclodehydration under sequential temperature programming (90 °C/2h, 150 °C/1h, 200 °C/1h, 250 °C/30 min, and 300 °C/30 min). Finally, the PI film was stripped off the glass substrate after being soaked in deionized water and further dried in a convection oven at 70 °C for 6 h.

2.3. Laser driven large area nanocarbon micropatterning

Large area (1.27 cm × 1.27 cm) micropattern arrays of LINC were generated on PI substrates (average thickness of 70 μm) using a 10.6 μm CO_2 IR continuous-wave laser(Full Spectrum Laser Pro-Series 20x12 platform, 1.5 in. focus lens). A single LINC array is formed by controlled laser rastering at vertically fixed sample stage (sample fixed at beam waist) under ambient conditions. Lasing proceeds along the positive X-direction for a certain distance (L_x) at raster speed (v), then shifting by an increment (p) in the Y-direction, followed by lasing in the negative X-direction for the same distance (L_x), as illustrated schematically in Fig. 4 (a). This sequence is rapidly repeated during rastering until the array of lines is completed. RentinaEngrave 3D software is used to programe the parameters on the laser machine, and a MATLAB script was written to generate the input design files with lines and a certain number of pixels for gap between lines in a single array. The laser texturing was operated at 12.5 W of laser power with X-direction raster speed of 491 mm s^{-1}. Programmed line spacing has been adjusted between 1 and 9 pixels (with increments of 3), where one pixel represents a shift of 50.8 μm. These translate to line pitch values of 101.6, 203.2, 355.6, and 508 μm. The chemical composition-driven laser-written lines are denoted as N-LINC for PMDA − ODA and F-LINC for 6FDA − TFMB, respectively.

2.4. Beam proximity effect model

To understand the effect of changing the lasing line pitch (p) on the fluence and cumulative fluence delivered to the PI films, we developed an elliptical Gaussian beam model (assuming single mode operation and full surface absorption). The laser beam profile and power were previously estimated experimentally using the knife-edge technique. [30] The laser beam flux (I) is expressed at a point (x, y) at the laser beam focus and time (t) using scanning in the x-direction with speed (v) according to the following expression:

$$I(x,y,t) = \frac{2P}{\pi w_{ox} w_{oy}} e^{-\left(\frac{2(x-(L_x-vt))^2}{w_{ox}^2}+\frac{2y^2}{w_{oy}^2}\right)}$$

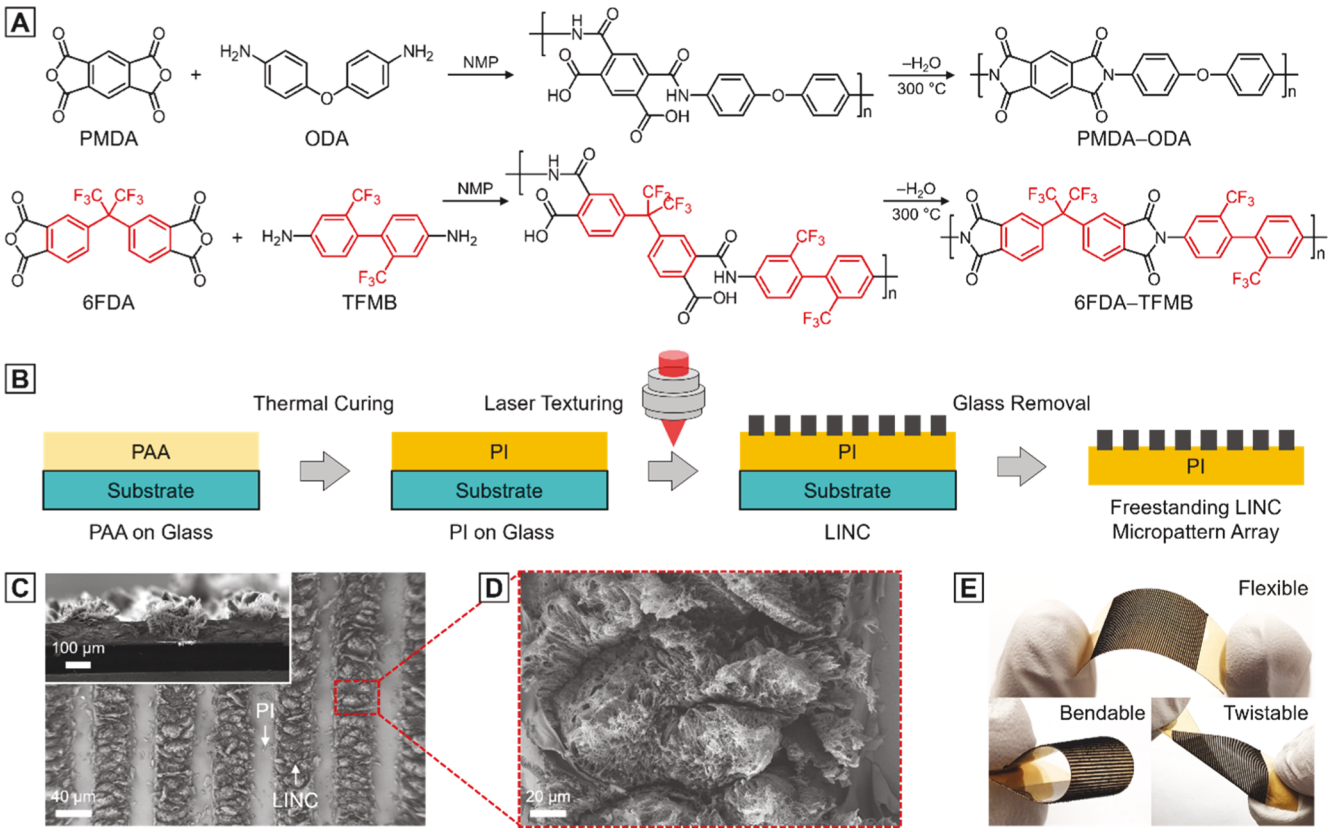

Fig. 1. Laser direct texturing of heteroatom-doped LINC micropatterns on PI films. (a) Synthetic route and chemical structures of PIs: PMDA–ODA to produce N-LINC, and 6FDA–TFMB to produce F-LINC. (b) Fabrication schematics of freestanding PI films with LINC micropatterns. (c) SEM image of F-LINC micropatterns obtained at laser fluence of 16 J cm^{-2} with line pitch of 355.6 μm. Inset shows cross-sectional SEM image. (d) SEM image of the close-up micropattern surface area of F-LINC with swollen porous microstructural hierarchies. (e) Deomistration of the mehcnaical flexibility of the PI films, and the robustness of the laser-produced F-LINC micropatterns on 6FDA − TFMB.

where P is the laser beam power, w_{ox} and w_{oy} is the beam waist size, v is the beam velocity and L_x is the lasing length in the x-direction.

To estimate the fluence at a point, the × and y-values are fixed at a point (x_o,y_o) and the flux is integrated over time using the following expression:

$$F(t) = \int_0^{\infty} I(x_o, y_o, t)dt$$

If this value is estimated at different y-values perpendicular to the laser path, the fluence (F) delivered across the sample can be estimated due to a single laser path. When the laser rasters across the sample, this fluence distribution shifts, and depending on the line pitch, overlapping between the successive laser passes can occur. A superposition of the fluence of the different passes during rastering is used to estimate the cumulative fluence (F_c) at differeent locations.

2.5. Measurements

Attenuated total reflection − Fourier transform-infrared (ATR-FTIR) spectra were obtained with a Bruker VERTEX-70LS. Thermogravimetric analysis (TGA) and differential scanning calorimetry (DSC) were conducted with a simultaneous thermal analyzer STA 6000 under N_2 flow at a heating rate of 10 °C min^{-1}. Scanning electron microscopy (SEM) images were obtained with a Zeiss SIGMA VP high resolution field emission instrument at an acceleration voltage of 2 kV. X-ray photoelectron spectroscopy (XPS) measurements were performed using a Kα-spectrometer equipped with an Al − Kα micro-focused monochromator. Raman spectra were recorded on a Renishaw Raman microscope using a 633 nm laser excitation at room temperature with a laser power of 5 mW. X-ray diffraction (XRD) was conducted on a Bruker D8 Discover SRD X-ray diffractometer with Cu Kα radiation (λ = 1.54 Å). Surface wettability was analyzed by measuring the Young-Laplace's CA using the sessile drop method at ambient temperature (~23 °C) in air by Biolin Scientific Attention Theta optical tensiometer. The CAs were recorded with a droplet volume of 5 μL after 3 s from droplet deposition. The sliding behaviors were evaluated by using automated tilting control of the goniometer stage at a rate of 1°/s. Calculating the number of replicates for CA values were at least 10. For each reported value, all the measurements taken from different surface locations were averaged and the standard deviation was calculated. These replicates ensured that any small batch differences did not influence the reported results. The surface roughness parameters and surface energy of micropatterns were characterized by using an Attention 3D topography module combined with optical tensiometer. The scanning area was 3.2 × 2.8 mm.

3. Results and discussion

We use the term laser-induced nanocarbon (LINC) to collectively refer to all the types of morphologies produced by laser carbonization of polymer precursors, including our well-ordered micropatterns consisting of hierarchical graphene-based networks in this work. Moreover, we use the acronym F-LINC to refer to the flourine-doped LINC produced by direct laser irradition of fourinated aromatic PI films of 6FDA − TFMB (more details in the experimental section and in Fig. 1) in air without any external doping sources or post-processing steps (either through controlling gas atmosphere or using additive chemicals). Similarly, we refer to LINC obtained by carbonization of PMDA–ODA as N-LINC, owing to the observed nitrogen doping (more details below). A series of

PIs with different molecular building blocks were synthesized by the conventional two-step procedure of ring-opening polyaddition and subsequent thermal cyclic dehydration (Fig. 1(a)). [47] To create the micropatterns (Fig. 1(b)), poly(amic acid) (PAA) intermediate solution was cast on a glass substrate and cured by stepwise thermal imidization procedure at 300 °C (see Supplementary Fig. S1(a)–(b)). The PI coated on glass substrate was irradiated by a moving CO_2 laser beam (10.6 μm wavelength) under ambient conditions. Using computer-aided control of parameters during laser scaning and rastering, large area LINC micropatterns are precisely controlled in terms of both geometry (line shape, size and spacing) and morphology.

To understand the process-strucutre relationship, we created maps correlating laser parameters like power and speed to the morphology and quality of the carbonized lines on PI films (see Supplementary Fig. S2). Each cell of the map corresponds to a certain combination of laser power and raster speed, and the color of the cell identifies the morphology/phase observed. In the map, we distinguish five different morphologies/phases and the determine the values of power and speed neccessary to transition between them: (i) non-graphitization (yellow region), where laser fluence is too low to adequately carbonize the PI; (ii) uniform and continuous porous line (green region), where adequate carbonization of PI; (iii) wooly nanofibers (red region), where a fluffy disconuous line is less well-defined; (iv) serpentine line or delamination (gray region), where the fluence is high enough to caues delmaination, but not ablation of the carboized line; and (v) complete line cut (black region), where laser fluence is high enough to cause ablation. In general, an increase in laser fluence achieved high graphitization, but the pattern became increasingly more brittle. Hence, there is a trade-off between graphitization and mechanical stability, and we optimized the laser parameters accordingly. SEM imaging in Fig. 1(c) and (d) clearly shows the period patrerning induced by laser scribing the PI film using a programmed line pitch. Fig. 1(d) also shows a magnified SEM image of the local area of F-LINC with uniformly swollen porous microstructural hierarchies. Importantly, the F-LINC micropatterns produced on 6FDA − TFMB films were mechanically stable and showned no signs of delamination of cracking upon severe bending and twisting, i.e. F-LINC micropatterns could retain their original shape and structural integrity even after releasing the applied bending and twisting loads (Fig. 1(e)).

Precise tuning of the directional surface patterns was achieved by adjusting the programmed scan line pitch (p) between lines within each periodic array, while maintaining a constant line width (w). This is acheived by programing the number of pixels for line width and spacings, condiering that one pixel represents a shift of 50.8 μm in our setup. Hence, the micro-scale striped patterns are formed rapidly in a single step as the laser is rastered along the main axis and shifted in the direction perpedicular to the main axis of lasing. Schematic images of surface geometry are shown in Fig. 2(a) along with detailed geometric parameters of the striped micropatterns.

The morphological difference in the striped LINC surfaces area observed depending on the programmed line pitch, as shown in the SEM images. Individual LINC lines were created down to a minimum width of 175 μm by scribing with a laser beam spot with a nominal diameter of 168 μm. Small differences between the nominal beam size and the actual size of the scribed LINC lines is ascribed to the fact that the actual area affected by the carbonizing temperatures during laser pyrolysis differs based on the dynamics and spatial distirbution of optical energy density (or fluence), as well as on the thermal degradation behavior of the polymer. From SEM images shown in Fig. 2(b)–(i), we measured LINC line height of < 150 μm. As expected, the experimental values for pitch and line spacing dimensions increased with increasing programmed scan line pitch (p), while the effective average line width has been constant for each type of PI (i.e. LINC line width is independent of line

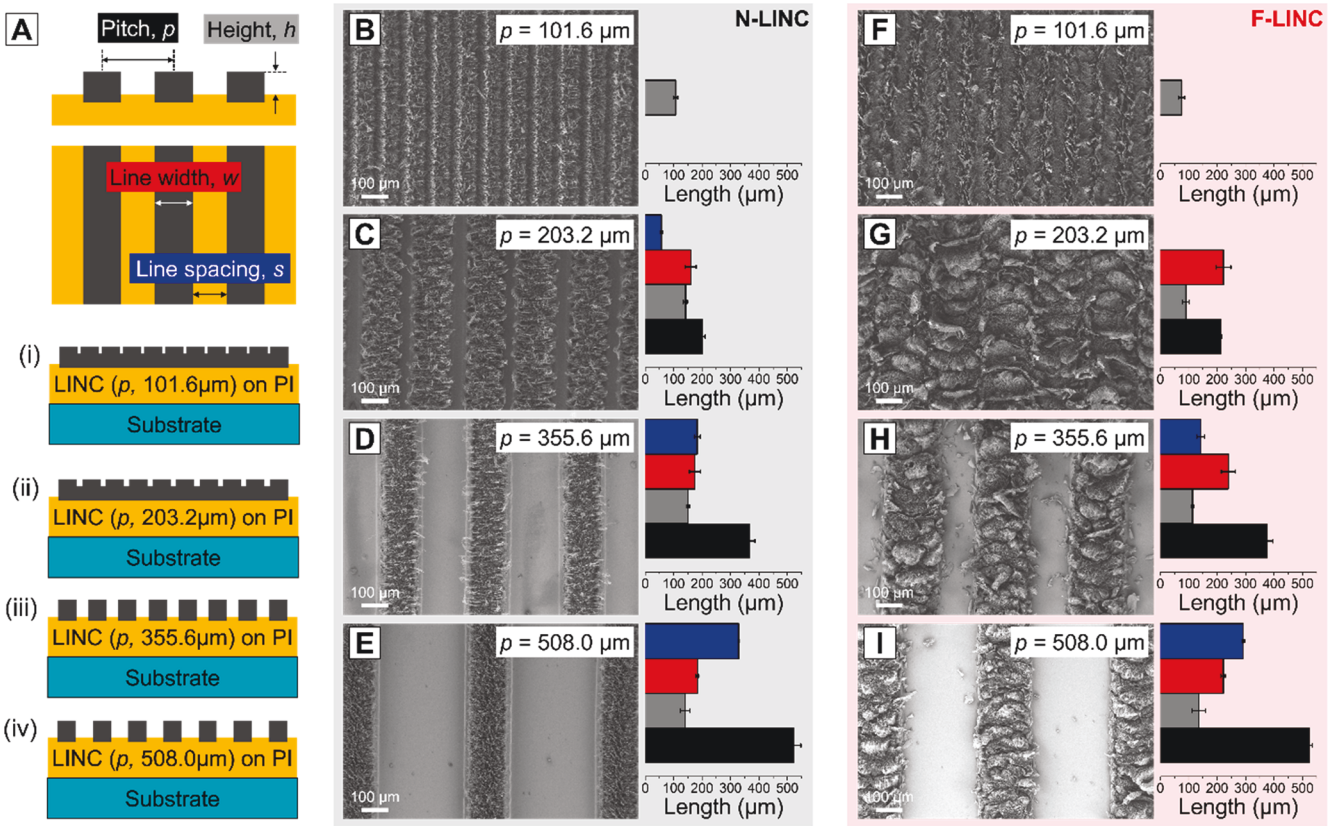

Fig. 2. Development of heteroatom-doped LINC having different micropattern geometry. (a) Schematic diagrams of LINC micropatterns showing geometric parameters. Surface morphology and carbon line dimensions of (b)–(e) N-LINC and (f)–(i) F-LINC micropatterns as represented by the SEM images and bar graphs, with blue representing the line spacing (s); red, line width (w); black, the center to center pitch (p); and gray, height of line (h).

pitch). We also observed that F-LINC exhibits larger line width of ~ 251 μm, compared to corresponding average line width of ~ 172 μm for N-LINC obtained at the same laser fluence. This difference between line widths of N-LINC and F-LINC highlights the differences in inherent thermal degradation behavior of the different PI films, which was confimed from thermogravimetric analysis (see Supplementary Fig. S1(c) and Table S1). The cross-sectional SEM images (see Supplementary Fig. S3) show LINC micropatterns of an ordered hierarchical porous morphology composed of continuous cellular networks. F-LINC lines are more textured than N-LINC, because the laser carbonization of 6FDA − TFMB is concomitant with thermal expansion and the liberation of various gaseous decomposition products (−CF, $-CF_3$ − CHF_2, $-CH_2F$, and − COF_2) during the transient local photothermal reactions, [48,49] which is also supported by the lower percentage of carbonized residue at 800 °C ($char_{800}$) of 6FDA − TFMB (53.5%) compared to PMDA–ODA (59.6%) (see Supplementary Fig. S1 (c) and Table S1).

The dependence of the surface roughness of LINC micropatterns on the line pitch is presented in Fig. S4(a)−(b). The measurements were carried out using an optical tensiometer with 3D topography module (see Supplementary Fig. S4(c)−(d)). Both the arithmetic average roughness (S_a) and root-mean-square roughness (S_q) were largely contant for nonoverlaping lines (i.e. when the line width was smaller than the line pitch). On the other hand, due to the overlapping lines (i.e. line width larger than line pitch) in the case of $p = 101.6$ μm for both N-LINC and F-LINC (as well as in the case of $p = 203.2$ μm for F-LINC only), both S_a and S_q are less than half the values for micropatterns with non-overlaping lines (line-to-line pitch larger than line width). Thus, the degree of overlapping between adjacent lasing lines strongly affects surface topography, and these proximity effect also depend on the chemical structure of PI films (i.e comparing the less thermally stable 6FDA–TFMB to the more thermally stable PMDA–ODA).

To further understand how such proximity effects control the PI-to-LINC chemical transformation, we utlized X-ray phoroelectron spectroscopy (XPS) to systemically interrogate LINC micropatterns. Fig. 3 (a)−(b) (plotted from Supplementary Table S2) compare the XPS elemental compositions of both N-LINC and F-LINC micropatterns originated from PIs having different chemical structure. From XPS survey scans, for which the spectrums are plotted in Fig. S5, peaks located at binding energies of 283.5 eV, 398.9 eV, 531.4 eV, and 687.1 eV correspond to the C, N, O, and F atoms, respectively. [48,50] Our results show that the degree of graphitization and heteroatom doping level of LINC micropatterns can be readily controlled by changing the pitch of periodic patterns. For LINC micropatterns with different line pitches (101.6, 203.2, 355.6, and 508 μm) lased at the fixed laser fluence of 16 J cm^{-2}, the percentage of C sharply increased with smaller line pitch, while the atomic percentages of heteroatoms (N, O, or F) decreased precipitously. As line pitch increases, the high resolution F1s spectrum of the F-LINC clearly reveals C—F bonds with neighboring C atoms at 686.6 eV and 687.6 eV, which were associated with semi-ionic C—F and covalent C—F bonds (see Supplementary Fig. S5). The deconvolution of the C1s spectrum also reveals multiple carbon bonds in our F-LINC,

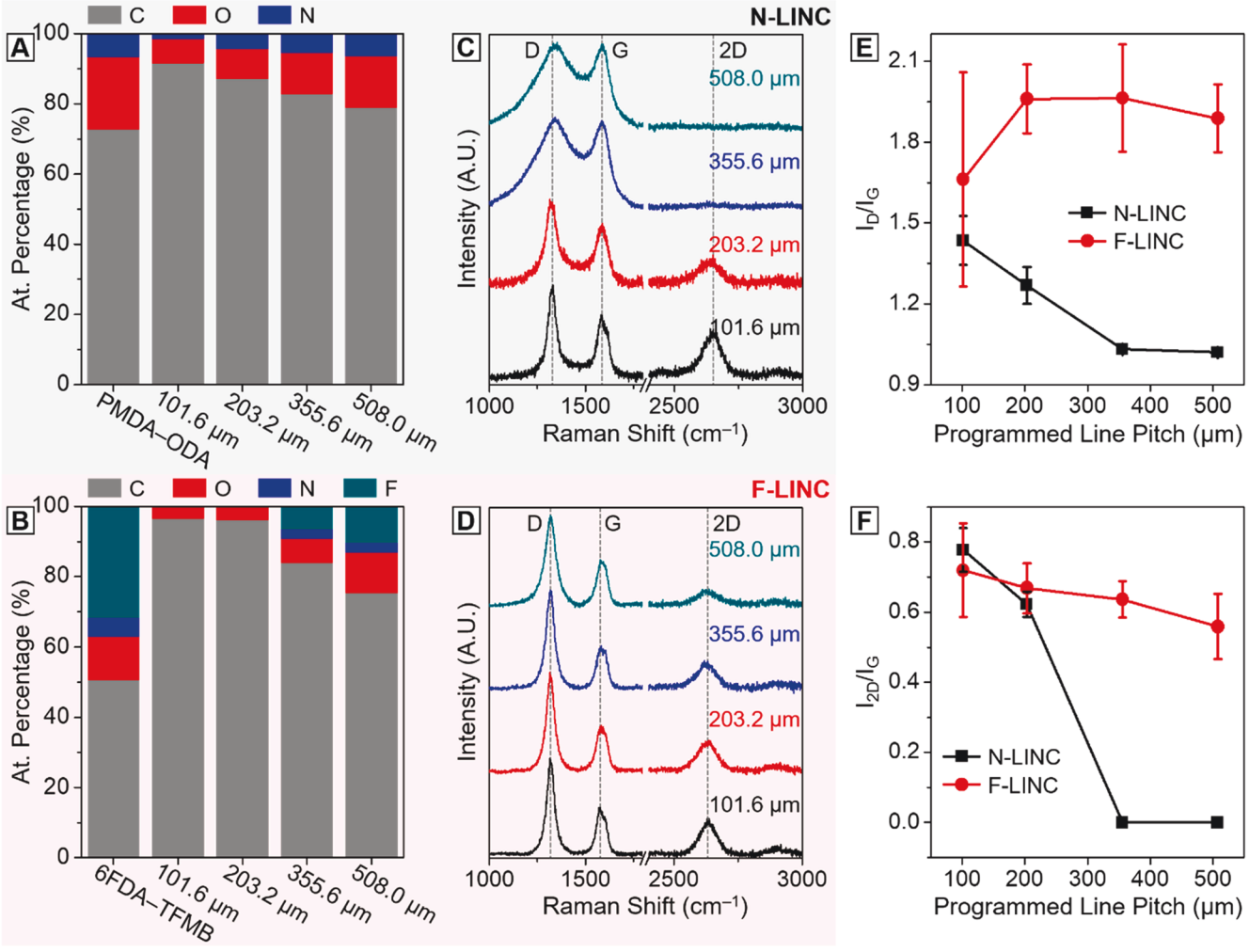

Fig. 3. Surface characterization of heteroatom-doped LINC micropatterns as a function of line pitch. XPS survey spectra of (a) N-LINC and (b) F-LINC micropatterns. Raman spectra of (c) N-LINC and (d) F-LINC micropatterns. (e) I_D/I_G and (f) I_{2D}/I_G ratio of N-LINC and F-LINC micropatterns.

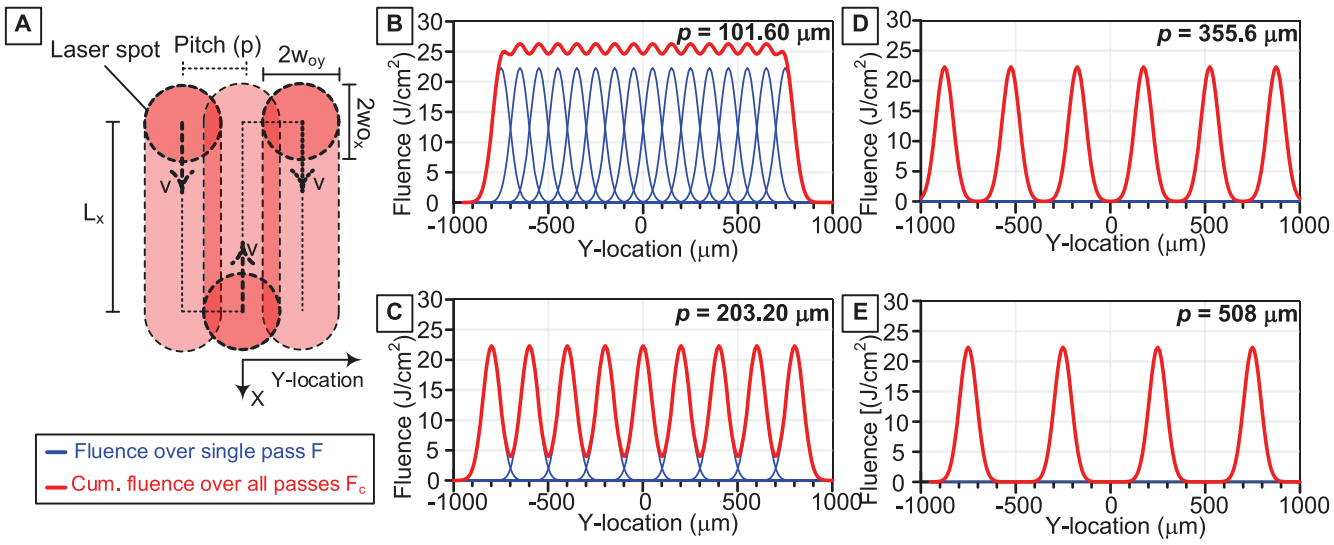

Fig. 4. (a) Schematic illustrating the rastering of the laser beam having spot size of $2w_{oy}$ and $2w_{ox}$. Here, the beam moves a distance (L_x) with speed v along the main lasing direction(X-direction), then the beam laterally shifts by a distance (p) along the Y-direction. This sequence is repeated until the designed micropattern is completed. Plots showing the fluence (F) and cumulative fluence after adding the effect of line overlap (F_c) for pitch values of (b) p = 101.6 μm, (c) p = 203.20 μm, (d) p = 355.6 μm, (e) p = 508 μm.

namely, the graphitic C—C at 284.6 eV, C—N at 285.6 eV, C—O at 286.1 eV, semi-ionic C—F at 287.5 eV, covalent C—F at 289.1 eV, O═C—O at 290.7 eV, and covalent C—F_2 at 292.5 eV, respectively. [51,52] Moreover, deconvolution of the characteristic C1s peaks of F-LINC with line pitch of 355.6 μm revealed that C—C bonds constituted more than 63% of the chemical bonds (see Supplementary Fig. S5). These results confirm that the F atoms are doped within the carbon frameworks without destroying or significantly weakening their aromaticity, and the remaining atoms are liberated in the form of gaseous decomposition products.

The Raman spectra displayed in Fig. 3(c)–(d) show three prominent bands: disorder-related D (~1350 cm^{-1}), first-order G (~1580 cm^{-1}), and second-order 2D (~2650 cm^{-1}) bands, which are characteristic peaks of sp^2 carbons. [53] Hence, the Raman spectra of all samples clearly demonstrate the presence of graphitic carbon. With decreasing the line pitch from 508 μm to 101.6 μm, the intensity of the 2D band increased monotonically, suggesting higher quality graphene with fewer defects. On the other hand, the significant broadening of the D and G bands and absence of a 2D band for N-LINC with large line pitches of 355.6 μm and 508 μm indicate a lower degree of graphitization and more structural defects in the cases of nonoverlapping N-LINC micropatterns. Fig. 3(e)–(f) show the quantified results of the D to G intensity ratio (I_D/I_G) and the 2D to G intensity ratio (I_{2D}/I_G) as metrics to evaluate the quality of sp^2 carbon in LINC. Since the intensity of the 2D band depends to a great extent on the electron/hole scattering rate, [54] which is affected by lattice defects as well as by charge carriers (which are boosted by heteroatom doping), the relatively high I_{2D}/I_G ratio for F-LINC compared to N-LNC despite the higher I_D/I_G ratio (especially for nonoverlapping line pitch values of 355.6 μm and 508 μm) is consistent with the effect of the charge carriers from F-doping, even if lattice defects and structural disorder are high (as indicated by the higher I_D/I_G). [55] It is worth noting here that the intensity of the D peak in F-LINC is generally stronger compared to that of N-LINC. This is explained by the greater disruption to the hexagonally ordered graphene lattice caused by the presence of F dopants compared to N dopants, owing to the larger mismatch of atomic size. Since the presence of defects, vacancies, edges, and other forms of lattice disorder in the sp^2 bonded carbon domain contribute to the D peak intensity, [56] our F-LINC exhibit an increases D-peak intensity. The F-containing groups in molecular backbones of 6FDA – TFMB are incorporated into the graphenic structure and excess F-derivatives (—CF, —CF_3—CHF_2, —CH_2F, and —COF_2) are released into the air during local laser irradiation. Therefore, the change in Raman intensity of D peak is associated with the sp^3-type defects caused by the occurrence of doping of F dopants into the hexagonal carbon framework. [57] These derived CF defects have the effect of buckling the carbon lattice. [58,59] In addition, the doping of F atoms in LINC leads to the formation of an energy band near the Fermi level, i.e., lead to a change in interatomic distances and consequent redistribution of electronic charge [59].

To elucidate the mechanism of the observed dependence of LINC surface chemistry and structure on line pitch, we model the proximity effects that result in excessive local heating in the vicinity of adjacent carbon lines when the lines overlap. Fig. 4(a) schematically illustrates the overlap of successive scans when the the laser beam is rastered back and forth during LINC micropattern fabrication. The spatial profiles of fluence calculated for each single laser pass are plotted as a function of the laterial Y-direction for different values of line pitch p in Fig. 4(b – e). Moreover, the cumulative fluence is also plotted by taking into consideration the superposition resulting from line overlaps, i.e. fluence values are added when lines overlap. Therefore, the spatial map of cumulative fluence over the lased area is representative of the local laser-induced heating, which drives graphitization during LINC formation. At the smallest line pitch (p = 101.6 μm), significant overlap is observed between the fluence (F) delivered by each adjacent lasing line, which boosts the cumulative fluence (F_c) significantly as shown in Fig. 4(b). It is also noted that the cumulative fluence is more homogeneous (with lower variations across the lateral Y-direction perpendicular to the main lasing direction) in this case of maximum line overlap. At a higher value of line pitch (p = 203.2 μm), there is still some overlap between the fluence delivered for the separate lasing lines (which is also reflected on the cumulative fluence), assuming the nominal beam size of 168 μm that translates into different line thickness depending of the PI chemistry as explained above. On the other hand, for the cases of nonoverlapping lines at higher line pitch values (p = 355.6 μm and p = 508 μm), the fluence and cummulative fleince profiles coinside, as there is no supersition, as shown in Fig. 4(d and e). Hence, these fluence calculations based on Gaussian beam modeling provide insights into the fluence-dependence of line proximity in periodic micropatterns, which manifests in the surface chemistry and morphology of the produced LINC.

We now quantitatively characterize the surface wettability of our well-ordered hierarchically porous LINC micropatterns by measuring

the CA formed by a water droplet at the three-phase boundary of solid – liquid – air. Water droplets wet the PMDA – ODA film surface owing to the relatively large surface free energy (see Supplementary Fig. S1(d) and Table S1), [60] while the fluorinated molecular building blocks in 6FDA – TFMB increased the CA of pristine PI film from 65° to 85°. When these PIfilm surfaces are textured with LINC micropatterns, the observed wetting behavior is influenced by the complexity of the anisotropic (and periodic) line features, as well as by hierarchical LINC morphology and chemical composition.

Fig. 5 and Table S3 show the results of static CAs of LINC micropatterns from different viewing directions in order to measrure the parallel CA ($\theta_{\parallel}$) and the perpendicular CA ($\theta_{\perp}$) to the direction of the lased lines (Fig. 5(a)). Although static $\theta_{\perp}$ and $\theta_{\parallel}$ follow a similar trend as a function of programmed line pitch, values for $\theta_{\perp}$ are consistently larger than values for $\theta_{\parallel}$. The difference in the wetting behavior in the two orthogonal directions arises from the anisotropic and highly directional nature of the pattern of periodic parallel lines. The water droplets, which adhered to the LINC surface, can spread in the parallel direction more freely than in the perpendicular direction. On the other hand, the droplets are pinned to the LINC lines and hence exhibit periodic stick–slip behavior along the perpendicular direction, along which that the spreading is suppressed by the contact line, [61,62] (resulting in a larger $\theta_{\perp}$ than $\theta_{\parallel}$).

Another important finding is that for highly overlapping lines at small line pitch (p = 101.6 μm), all LINC micropatterns exhibited hydrophillic wetting behavior that was less anisotropic than in the cases with nonoverlapping lines (p = 355.6 μm and p = 508 μm). This is explained by the more homogeneous LINC topography (smaller overall surface roughness and periodicity) and prorosity allowing water to impregnate the surface (Wenzel state). [63] Further increasing surface roughness enhances hydrophobicity of the LINC micropatterned surface.

It should be noted that the measured CAs in all F-LINC samples (Fig. 5(c)) were larger than that for N-LINC samples (Fig. 5(b)) at the same line pitch. Interestingly, by increasing line pitch to 355.6 μm, a superhydrophobic surface of F-LINC with a CA $\theta_{\perp}$ of 156° is obtained, and trapped air pockets between the ridges are clearly observed (inset image in Fig. 5(c)). This significant increase in droplet CA is ascribed to the low surface free energy created by the C—F bonds. Moreover, the inherent nano/micro-scale roughness of the hierarchically structured porous F-LINC micropatterns can lead to large increase in the Laplace pressure at the gas – liquid interface. [64] When the pixel pitch was greater than 355.6 μm however, the both CAs $\theta_{\perp}$ and $\theta_{\parallel}$ of F-LINC decreased from 156° to 141° and from 135° to 91°, respectively, indicating that the liquid – air interface collapsed due to sufficiently large line spacing and liquid pressure.

To shed more light on the adhesion of water droplets to our LINC micropatterns, we chracterize the dynamic CAs of water droplets on tilted samples. Fig. 6 and Table S4 – S5 illustrate the variations of advancing angle (θ_A), receding angle (θ_R), and CA hysteresis ($\Delta\theta = \theta_A - \theta_R$) corresponding to different values of line pitch. The CA hysteresis, generally caused by surface roughness and anisotropy, refers to the energy dissipated during the physical movement of the droplet along a surface. [65,66] Typically, a surface is considered to be water-repellent when it exhibits high CA with low CA hysteresis for a contacting droplet. [67] In contrast to such water-repellent surfaces, the "sticky non-wetting surface" exhibits high CA and high CA hysteresis, exhibiting parahydrophobic behavior, known as "rose petal effect" [68,69].

The work of adhesion to water droplet for the LINC micropatterned surfaces is governed by the CA hysteresis caused by the kinetic barrier difference in the advancing and receding modes. [62] Fig. 6(b) and (d) show that θ_A, θ_R, and CA hysteresis are generally proportional to the surface roughness, especially for $\theta_{\perp}$. Similar to the results of static CAs shown in Fig. 5, the results of dynamic CAs on vertical samples show that $\theta_{\perp}$ is larger than $\theta_{\parallel}$, for both advancing and receding angles of each orientation. The shapes of different water droplets on tilted samples (90°) is shown in Fig. 6(a) and (c). While there are differences in the values of hysteresis of contact angle as a function of line pitch, which indicate differences in adhesion, the droplets placed on all our LINC micropatterned surfaces maintain adhesion against gravityeven if when the surface is tilted 90° (vertical) or 180° (updide down). When tilting in the direction to view $\theta_{\parallel}$, the contact area of the droplet becomes larger, indicating that the droplet spreads on the surface along the $\theta_{A\parallel}$ direction, compared to the static CA $\theta_{\parallel}$. This unidirectional spreading of droplets occurs prominently in N-LINC, which is ascribed to the generally higher water affinity and higher surface energy of N-LINC compared to F-LINC.

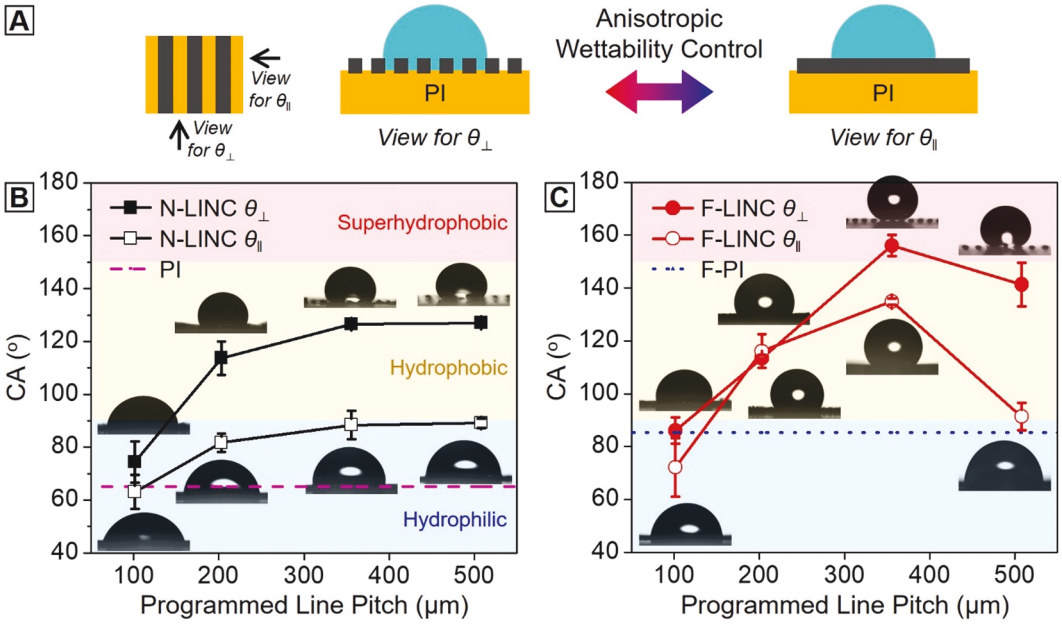

Fig. 5. Anisotropic wetting behavior of heteroatom-doped LINC micropatterns. (a) Schematic of viewing directions for measuring both the parallel CA ($\theta_{\parallel}$) and the perpendicular CA ($\theta_{\perp}$) to the direction of the lased lines. Plots of CAs of (b) N-LINC and (c) F-LINC micropatterns corresponding to different values of line pitch. Insets shows optical tensiometer images of water droplets, from which each measurement is obtained. Horizontal dashed lines represent the isotropic CA for the pristine PI film before laser carbonization.

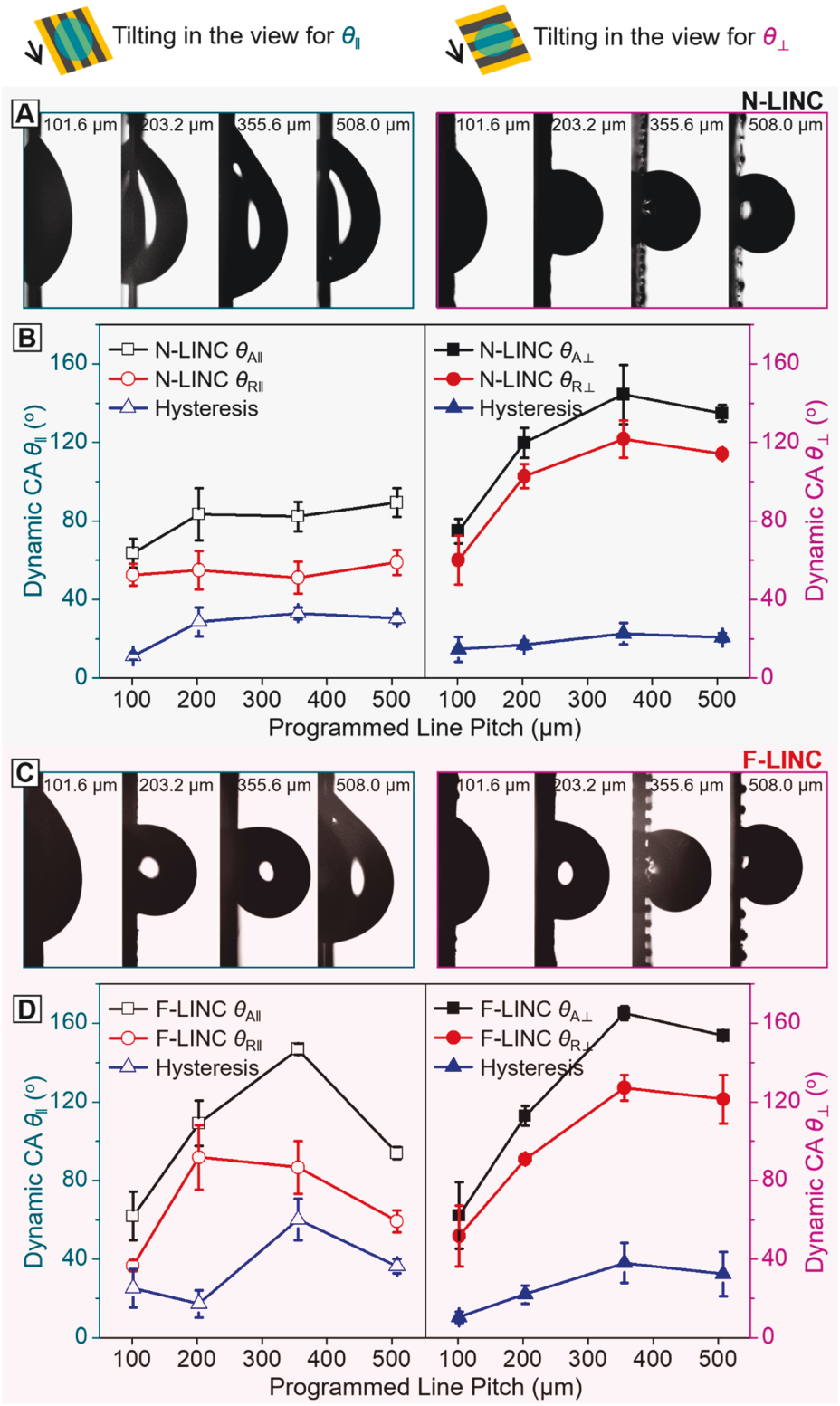

Fig. 6. Dynamic wetting behavior of heteroatom-doped LINC micropatterns. (a) Optical tensiometer images of water droplets on N-LINC tilted by 90°, and (b) plots of dynamic CAs and hysteresis values of N-LINC from different viewing directions. (c) Optical tensiometer images of water droplets on F-LINC tilted by 90°, and (d) plots of dynamic CAs and hysteresis values of F-LINC from different viewing directions. The notation θ_A and θ_R represent the advancing and receding angles.

Interestingly, the F-LINC sample with line pitch of 355.6 μmexhibits parahydrophobic surface, where the dynamic CAs along both perpendicular ($\theta_{A\perp} = 165°$, $\theta_{R\perp} = 127°$) and parallel ($\theta_{A\parallel} = 147°$, $\theta_{R\parallel} = 87°$) directions as well as the calculated CA hysteresis ($\Delta\theta_{\perp} = 38°$, $\Delta\theta_{\parallel} = 60°$) are high. This phenomenon manifests as an unusually high water droplet adhesion to the surface, despite the superhydrophobic state. Therefore, the droplets never roll-off the surface even when tilted by 90° or more. This parahydrophobic wetting behavior of F-LINC can be explained by a metastable Cassie – Baxter and Wenzel state referred to as the Cassie impregnating wetting state. [70,71] This wetting transition is ascribed

to the presence of both large features (the lines in our micropatterns), as well as nano/micro-scale hierarchical porous morphology of F-LINC in each line. The unique F-doped nanotexture of F-LINC results in the high static CA, whereas the larger scale lines that are sparce and low in height allow water to partially penetrate into the micropattern, resulting in high water adhesion [72,73].

Leveraging this unique rose-petal effect with surface adhesion and superhydrophobic properties of F-LINC micropatterns at line pitch of 355.6 μm, we proposed the use of these flexible samples for water droplet transportation without any loss or contamination. As shown in Fig. 7(c, (1)–(5)), a water droplet on a low adhesive superhydrophobic Teflon film could be easily picked up by flat F-LINC miropatterned sample, owing to the strong water adhesion force of the pinned superhydrophobic state. Upon bending the flexible sample, curvature-driven air injection into the micropattern arrays contributes to decreasing the water adhesion, enabling the release of the droplet (Fig. 7(a)). Increasing the curvature, which is enabled by the excellent flexibility of the PI film, reduces adhesion by transitioning toward the Cassie superhydrophobic state.[74,75] As shown in Fig. 7(c, (6)–(10)), the water droplet on the curved F-LINC surface (Fig. 7(b)) can be completely transferred to high adhesion surface, such as another flat F-LINC micropatterned PI films. This pick-and-place process is possible because the adhesion between the droplet and the curved sample is less than the adhesion between the droplet and the flat F-LINC. *In situ* manipulation of droplets using the strain-induced swithcing of adhesion is promising for various application in microfluidics, biomedical devices, and other site-specific release chemicals.

As a result, the impact of this study on scalable patterning of fluorinated graphene for functional anisotropic surfaces directly on flexible polyimide is remarkable in comparison with the results reported in the literature, as shown in Table S6. [34,35,37,76-79] Based on different surface characteristics including parahydrophobicity, mechanical-strain-induced switchable wettability, and droplet pick-and-place demonstration, it should be emphasized that the newly designed responsive F-LINC micropattern surface is potentially useful for lab-on-a-chip devices, especially for molecular detection, diagnostics, and cell biology applications.

4. Conclusion

We demonstrate a direct-write laser-based method to fabricate micropatterns of fluorine-doped graphene directly on flexible polymer films. Such textured surfaces exhibit superhydrophobicity, controllable water adhesion, and anisotropic wetting. In particular, we prepared periodic arrays of LINC lines by laser-induced graphene using an infrared continuous-wave laser on molecularly designed polyimide films. Compared with the N-LINC derived from PMDA – ODA, the large quantity of F-containing functional groups in 6FDA – TFMB resulted in abundant release of gaseous decomposition products during a transient local photothermal reaction, resulting in the formation of highly hierarchical nano/micro-structures with varying levels of F-doping up to 10.4% in F-LINC. The static CAs of water droplets on F-LINC micropatterned surfaces are consistently higher than those for N-LINC and exhibit superhydrophobicity (up to 156°) at programmed line pitch of 355.6 μm in the direction perpendicular to patterns. Additionally, F-LINC micropatterned PI samples also exhibit a "rose petal effect" manifests as strong adhesion between the water droplet and the textured surface, although the contact angle is above 150°, i.e., dynamic CAs in perpendicular ($\theta_{A\perp} = 165°$, $\theta_{R\perp} = 127°$) and parallel ($\theta_{A\parallel} = 147°$, $\theta_{R\parallel} = 87°$) direction, and anisotropic CA hysteresis ($\Delta\theta_{\perp} = 38°$, $\Delta\theta_{\parallel} = 60°$). These sticky parahydrophobic surfaces can be used as smart "mechanical hand" for droplet transportation by modulation of adhesion through strain-induced curvature control. Hence, our approach provides a facile and scalable surface engineering approach, applicable to flexible device manufacturing with tunability of surface wetting and adhesion and suitable for various droplet manipulation needs.

CRediT authorship contribution statement

Ki-Ho Nam: Conceptualization, Methodology, Investigation, Visualization, Writing – original draft. **Moataz Abdulhafez:** Investigation, Visualization, Writing–original draft. **Golnaz Najaf Tomaraei:** Investigation. **Mostafa Bedewy:** Conceptualization, Supervision, Visualization, Validation, Funding acquisition, Project administration, Writing – review & editing.

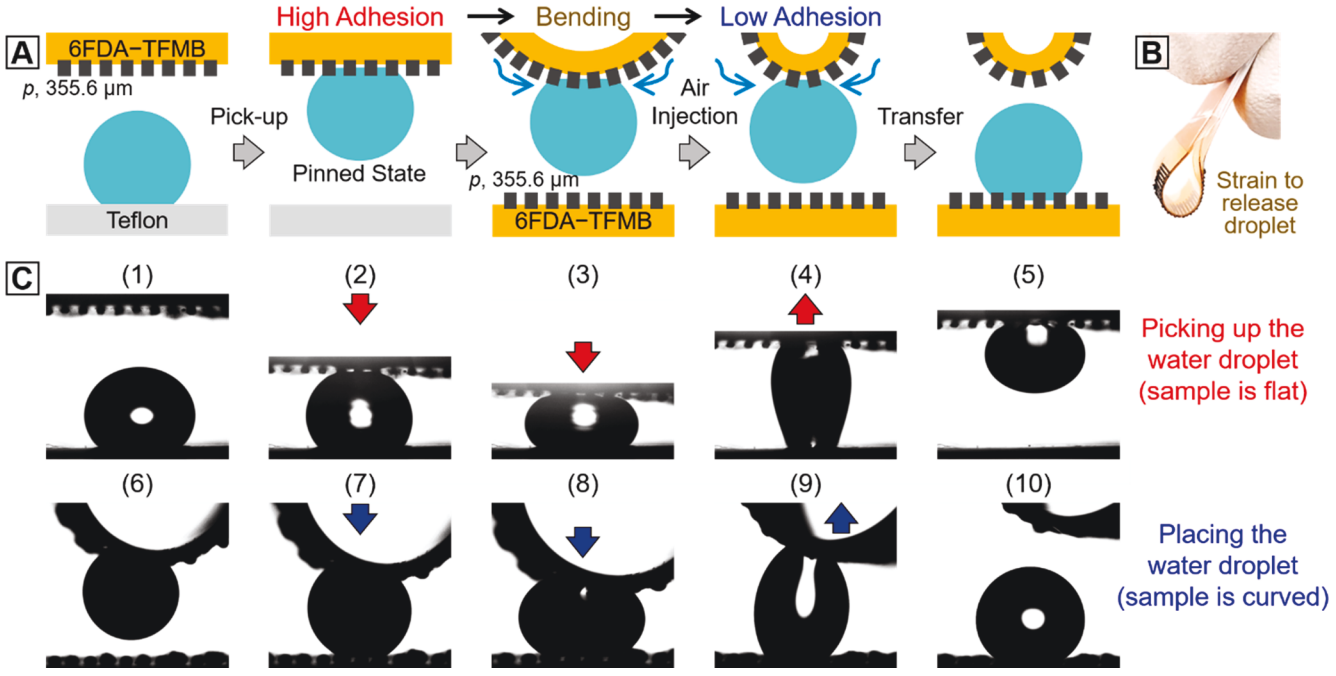

Fig. 7. Manipulation of a water droplet assisted by F-LINC micropatterns with a line pitch of 355.6 μm. (a) Scheme for transport of a water droplet through strain-induced reversible switching of droplet adhesion. (b) Photograph of curved/bent sample of F-LINC micropatterns for release of droplet. (c) Sequential optical tensiometer images showing the capture/pick-up of 5 μL water droplet (top, (1)–(5)) and the complete release of the droplet (bottom, (6)–(10)).

Declaration of Competing Interest

The authors declare that they have no known competing financial interests or personal relationships that could have appeared to influence the work reported in this paper.

Acknowledgements

This research was supported by the National Science Foundation (NSF) under award number 2028580 (any opinions, findings, and conclusions or recommendations expressed in this material are those of the author(s) and do not necessarily reflect the views of the NSF). Research was also supported by Pitt Momentum Seed grant and by the Department of Industrial Engineering at the University of Pittsburgh. Characterization was performed, in part, at the Nanoscale Fabrication and Characterization Facility, a laboratory of the Gertrude E. and John M. Petersen Institute of NanoScience and Engineering, housed at the University of Pittsburgh, and in part, at Materials Characterization Laboratory, housed at Department of Chemistry in the University of Pittsburgh.

Appendix A. Supplementary material

Supplementary data to this article can be found online at https://doi.org/10.1016/j.apsusc.2021.151339.

References

[1] X. Tian, T. Verho, R.H.A. Ras, Moving superhydrophobic surfaces toward real-world applications, Science (80-.) 352 (2016) 142–143, https://doi.org/10.1126/science.aaf2073.
[2] B. Su, Y.e. Tian, L. Jiang, Bioinspired Interfaces with Superwettability: From Materials to Chemistry, J. Am. Chem. Soc. 138 (6) (2016) 1727–1748, https://doi.org/10.1021/jacs.5b12728.
[3] T. Mouterde, G. Lehoucq, S. Xavier, A. Checco, C.T. Black, A. Rahman, T. Midavaine, C. Clanet, D. Quéré, Antifogging abilities of model nanotextures, Nat. Mater. 16 (6) (2017) 658–663, https://doi.org/10.1038/nmat4868.
[4] H. Liu, Y. Wang, J. Huang, Z. Chen, G. Chen, Y. Lai, Bioinspired Surfaces with Superamphiphobic Properties: Concepts, Synthesis, and Applications, Adv. Funct. Mater. 28 (19) (2018) 1707415, https://doi.org/10.1002/adfm.v28.1910.1002/adfm.201707415.
[5] T. Sun, G. Qing, B. Su, L. Jiang, Functional biointerface materials inspired from nature, Chem. Soc. Rev. 40 (2011) 2909–2921, https://doi.org/10.1039/c0cs00124d.
[6] S. Yang, J. Ju, Y. Qiu, Y. He, X. Wang, S. Dou, K. Liu, L. Jiang, Peanut leaf inspired multifunctional surfaces, Small. 10 (2) (2014) 294–299, https://doi.org/10.1002/smll.v10.210.1002/smll.201301029.
[7] P. Fan, R. Pan, M. Zhong, Ultrafast Laser Enabling Hierarchical Structures for Versatile Superhydrophobicity with Enhanced Cassie-Baxter Stability and Durability, Langmuir. 35 (51) (2019) 16693–16711, https://doi.org/10.1021/acs.langmuir.9b02986.
[8] Z. Zhou, T. Gao, S. McCarthy, A. Kozbial, S. Tan, D. Pekker, L. Li, P.W. Leu, Parahydrophobicity and stick-slip wetting dynamics of vertically aligned carbon nanotube forests, Carbon N. Y. 152 (2019) 474–481, https://doi.org/10.1016/j.carbon.2019.06.012.
[9] S.M. Kang, I. You, W.K. Cho, H.K. Shon, T.G. Lee, I.S. Choi, J.M. Karp, H. Lee, One-step modification of superhydrophobic surfaces by a mussel-inspired polymer coating, Angew. Chemie - Int. Ed. 49 (49) (2010) 9401–9404, https://doi.org/10.1002/anie.201004693.
[10] Y. Zuo, L. Zheng, C. Zhao, H. Liu, Micro-/Nanostructured Interface for Liquid Manipulation and Its Applications, Small. 16 (9) (2020) 1903849, https://doi.org/10.1002/smll.v16.910.1002/smll.201903849.
[11] C.R. Szczepanski, F. Guittard, T. Darmanin, Recent advances in the study and design of parahydrophobic surfaces: From natural examples to synthetic approaches, Adv. Colloid Interface Sci. 241 (2017) 37–61, https://doi.org/10.1016/j.cis.2017.01.002.
[12] K. Nagato, N. Takahashi, T. Shimura, M. Nakao, Droplet sliding behaviour on textured and fluorinated surface, CIRP Ann. 68 (1) (2019) 587–590, https://doi.org/10.1016/j.cirp.2019.04.038.
[13] D. Öner, T.J. McCarthy, Ultrahydrophobic surfaces. Effects of topography length scales on wettability, Langmuir 16 (20) (2000) 7777–7782, https://doi.org/10.1021/la000598o.
[14] H. Notsu, W. Kubo, I. Shitanda, T. Tatsuma, Super-hydrophobic/super-hydrophilic patterning of gold surfaces by photocatalytic lithography, J. Mater. Chem. 15 (2005) 1523–1527, https://doi.org/10.1039/b418884e.
[15] D. Zhu, X. Li, G. Zhang, X. Zhang, X. Zhang, T. Wang, B. Yang, Mimicking the rice leaf-from ordered binary structures to anisotropic wettability, Langmuir. 26 (17) (2010) 14276–14283, https://doi.org/10.1021/la102243c.
[16] H.E. Jeong, R. Kwak, J.K. Kim, K.Y. Suh, Generation and self-replication of monolithic, dual-scale polymer structures by two-step capillary-force lithography, Small. 4 (11) (2008) 1913–1918, https://doi.org/10.1002/smll.v4:1110.1002/smll.200800151.
[17] A. Pozzato, S.D. Zilio, G. Fois, D. Vendramin, G. Mistura, M. Belotti, Y. Chen, M. Natali, Superhydrophobic surfaces fabricated by nanoimprint lithography, Microelectron. Eng. 83 (4-9) (2006) 884–888, https://doi.org/10.1016/j.mee.2006.01.012.
[18] J. Gao, Y. Liu, H. Xu, Z. Wang, X.i. Zhang, Mimicking biological structured surfaces by phase-separation micromolding, Langmuir. 25 (8) (2009) 4365–4369, https://doi.org/10.1021/la9008027.
[19] J.-N. Wang, Y.-L. Zhang, Y. Liu, W. Zheng, L.P. Lee, H.-B. Sun, Recent developments in superhydrophobic graphene and graphene-related materials: From preparation to potential applications, Nanoscale. 7 (16) (2015) 7101–7114, https://doi.org/10.1039/C5NR00719D.
[20] C. Zhu, T.Y.J. Han, E.B. Duoss, A.M. Golobic, J.D. Kuntz, C.M. Spadaccini, M. A. Worsley, Highly compressible 3D periodic graphene aerogel microlattices, Nat. Commun. 6 (2015) 1–8, https://doi.org/10.1038/ncomms7962.
[21] L. Vertuccio, F. De Santis, R. Pantani, K. Lafdi, L. Guadagno, Effective de-icing skin using graphene-based flexible heater, Compos. Part B Eng. 162 (2019) 600–610, https://doi.org/10.1016/j.compositesb.2019.01.045.
[22] M.W. Jung, S.M. Kang, K.H. Nam, K.S. An, B.C. Ku, Highly transparent and flexible NO 2 gas sensor film based on MoS 2 /rGO composites using soft lithographic patterning, Appl. Surf. Sci. 456 (2018) 7–12, https://doi.org/10.1016/j.apsusc.2018.06.086.
[23] R. Ye, Y. Chyan, J. Zhang, Y. Li, X. Han, C. Kittrell, J.M. Tour, Laser-Induced Graphene Formation on Wood, Adv. Mater. 29 (37) (2017) 1702211, https://doi.org/10.1002/adma.v29.3710.1002/adma.201702211.
[24] Y. Chyan, R. Ye, Y. Li, S.P. Singh, C.J. Arnusch, J.M. Tour, Laser-Induced Graphene by Multiple Lasing: Toward Electronics on Cloth, Paper, and Food, ACS Nano. 12 (3) (2018) 2176–2183, https://doi.org/10.1021/acsnano.7b0853910.1021/acsnano.7b08539.s001.
[25] B. Kulyk, B.F.R. Silva, A.F. Carvalho, S. Silvestre, A.J.S. Fernandes, R. Martins, E. Fortunato, F.M. Costa, Laser-Induced Graphene from Paper for Mechanical Sensing, ACS Appl. Mater. Interfaces. 13 (8) (2021) 10210–10221, https://doi.org/10.1021/acsami.0c20270.
[26] A.F. Carvalho, A.J.S. Fernandes, R. Martins, E. Fortunato, F.M. Costa, Laser-Induced Graphene Piezoresistive Sensors Synthesized Directly on Cork Insoles for Gait Analysis, Adv. Mater. Technol. 5 (12) (2020) 2000630, https://doi.org/10.1002/admt.v5.1210.1002/admt.202000630.
[27] Y. Huang, L. Zeng, C. Liu, D. Zeng, Z. Liu, X. Liu, X. Zhong, W. Guo, L. Li, Laser Direct Writing of Heteroatom (N and S)-Doped Graphene from a Polybenzimidazole Ink Donor on Polyethylene Terephthalate Polymer and Glass Substrates, Small. 14 (44) (2018) 1803143, https://doi.org/10.1002/smll.v14.4410.1002/smll.201803143.
[28] J. Lin, Z. Peng, Y. Liu, F. Ruiz-Zepeda, R. Ye, E.L.G.G. Samuel, M.J. Yacaman, B. I. Yakobson, J.M. Tour, Laser-induced porous graphene films from commercial polymers, Nat. Commun. 5 (2014) 5714, https://doi.org/10.1038/ncomms6714.
[29] R. Ye, D.K. James, J.M. Tour, Laser-Induced Graphene: From Discovery to Translation, Adv. Mater. 31 (1) (2019) 1803621, https://doi.org/10.1002/adma.v31.110.1002/adma.201803621.
[30] M. Abdulhafez, G.N. Tomaraei, M. Bedewy, Fluence-Dependent Morphological Transitions in Laser-Induced Graphene Electrodes on Polyimide Substrates for Flexible Devices, ACS Appl. Nano Mater. 4 (3) (2021) 2973–2986, https://doi.org/10.1021/acsanm.1c00101.
[31] L.X. Duy, Z. Peng, Y. Li, J. Zhang, Y. Ji, J.M. Tour, Laser-induced graphene fibers, Carbon N. Y. 126 (2018) 472–479, https://doi.org/10.1016/j.carbon.2017.10.036.
[32] A.F. Carvalho, A.J.S. Fernandes, C. Leitão, J. Deuermeier, A.C. Marques, R. Martins, E. Fortunato, F.M. Costa, Laser-Induced Graphene Strain Sensors Produced by Ultraviolet Irradiation of Polyimide, Adv. Funct. Mater. 28 (52) (2018) 1805271, https://doi.org/10.1002/adfm.201805271.
[33] Z. Chen, L. Dong, D. Yang, H. Lu, Superhydrophobic graphene-based materials: Surface construction and functional applications, Adv. Mater. 25 (37) (2013) 5352–5359, https://doi.org/10.1002/adma.201302804.
[34] J. Nasser, J. Lin, L. Zhang, H.A. Sodano, Laser induced graphene printing of spatially controlled super-hydrophobic/hydrophilic surfaces, Carbon N. Y. 162 (2020) 570–578, https://doi.org/10.1016/j.carbon.2020.03.002.
[35] C.M. Tittle, D. Yilman, M.A. Pope, C.J. Backhouse, Robust Superhydrophobic Laser-Induced Graphene for Desalination Applications, Adv. Mater. Technol. 3 (2018) 1–10, https://doi.org/10.1002/admt.201700207.
[36] M. Abdulhafez, A.J. McComb, M. Bedewy, Tailoring Surface Hydrophobicity of Commercial Polyimide by Laser-Induced Nanocarbon Texturing, J. Micro Nano-Manufacturing. 8 (2020), 031006, https://doi.org/10.1115/1.4048600.
[37] Y. Li, D.X. Luong, J. Zhang, Y.R. Tarkunde, C. Kittrell, F. Sargunaraj, Y. Ji, C. J. Arnusch, J.M. Tour, Laser-Induced Graphene in Controlled Atmospheres: From Superhydrophilic to Superhydrophobic Surfaces, Adv. Mater. 29 (27) (2017) 1700496, https://doi.org/10.1002/adma.v29.2710.1002/adma.201700496.
[38] D.X. Luong, K. Yang, J. Yoon, S.P. Singh, T. Wang, C.J. Arnusch, J.M. Tour, Laser-Induced Graphene Composites as Multifunctional Surfaces, ACS Nano. 13 (2019) 2579–2586, https://doi.org/10.1021/acsnano.8b09626.
[39] S.P. Singh, Y. Li, A. Be'er, Y. Oren, J.M. Tour, C.J. Arnusch, Laser-Induced Graphene Layers and Electrodes Prevents Microbial Fouling and Exerts

Antimicrobial Action, ACS Appl. Mater. Interfaces. 9 (21) (2017) 18238–18247, https://doi.org/10.1021/acsami.7b04863.
[40] S.P. Singh, S. Ramanan, Y. Kaufman, C.J. Arnusch, Laser-Induced Graphene Biofilm Inhibition: Texture Does Matter, ACS Appl. Nano Mater. 1 (4) (2018) 1713–1720, https://doi.org/10.1021/acsanm.8b00175.
[41] M.G. Stanford, J.T. Li, Y. Chen, E.A. McHugh, A. Liopo, H. Xiao, J.M. Tour, Self-sterilizing laser-induced graphene bacterial air filter, ACS Nano. 13 (10) (2019) 11912–11920, https://doi.org/10.1021/acsnano.9b05983.
[42] A.K. Thakur, S.P. Singh, M.N. Kleinberg, A. Gupta, C.J. Arnusch, Laser-Induced Graphene-PVA Composites as Robust Electrically Conductive Water Treatment Membranes, ACS Appl. Mater. Interfaces. 11 (11) (2019) 10914–10921, https://doi.org/10.1021/acsami.9b00510.
[43] A. Tiliakos, A.M.I. Trefilov, E. Tanasă, A. Balan, I. Stamatin, Laser-induced graphene as the microporous layer in proton exchange membrane fuel cells, Appl. Surf. Sci. 504 (2020) 144096, https://doi.org/10.1016/j.apsusc.2019.144096.
[44] W. Ma, J. Zhu, Z. Wang, W. Song, G. Cao, Recent advances in preparation and application of laser-induced graphene in energy storage devices, Mater. Today Energy. 18 (2020) 100569, https://doi.org/10.1016/j.mtener.2020.100569.
[45] Y. Yang, Y.u. Song, X. Bo, J. Min, O.S. Pak, L. Zhu, M. Wang, J. Tu, A. Kogan, H. Zhang, T.K. Hsiai, Z. Li, W. Gao, A laser-engraved wearable sensor for sensitive detection of uric acid and tyrosine in sweat, Nat. Biotechnol. 38 (2) (2020) 217–224, https://doi.org/10.1038/s41587-019-0321-x.
[46] A.R. Cardoso, A.C. Marques, L. Santos, A.F. Carvalho, F.M. Costa, R. Martins, M.G. F. Sales, E. Fortunato, Molecularly-imprinted chloramphenicol sensor with laser-induced graphene electrodes, Biosens. Bioelectron. 124–125 (2019) 167–175, https://doi.org/10.1016/j.bios.2018.10.015.
[47] K.-H. Nam, A. Lee, S.-K. Lee, K. Hur, H. Han, Infrared transmitting polyimides based on chalcogenide element-blocks with tunable high-refractive indices and broad optical windows, J. Mater. Chem. C. 7 (34) (2019) 10574–10580, https://doi.org/10.1039/C9TC03574E.
[48] M. Kim, M.G. Gu, H. Jeong, E. Song, J.W. Jeon, K.-M. Huh, P. Kang, S.-K. Kim, B. G. Kim, Laser Scribing of Fluorinated Polyimide Films to Generate Microporous Structures for High-Performance Micro-supercapacitor Electrodes, ACS Appl. Energy Mater. 4 (1) (2021) 208–214, https://doi.org/10.1021/acsaem.0c02096.
[49] N. Ohta, Y. Nishi, T. Morishita, T. Tojo, M. Inagaki, Preparation of microporous carbon films from fluorinated aromatic polyimides, Carbon N. Y. 46 (10) (2008) 1350–1357, https://doi.org/10.1016/j.carbon.2008.05.019.
[50] K.-H. Nam, U.i. Jung Kim, M. Hee Jeon, T.-R. Lee, J. Yu, N.-H. You, Y.-K. Kim, J. i. Won Suk, B.-C. Ku, Green, fast, and scalable production of reduced graphene oxide via Taylor vortex flow, Chem. Eng. J. 391 (2020) 123482, https://doi.org/10.1016/j.cej.2019.123482.
[51] R. Ye, X. Han, D.V. Kosynkin, Y. Li, C. Zhang, B.o. Jiang, A.A. Martí, J.M. Tour, Laser-Induced Conversion of Teflon into Fluorinated Nanodiamonds or Fluorinated Graphene, ACS Nano. 12 (2) (2018) 1083–1088, https://doi.org/10.1021/acsnano.7b05877.
[52] M. Ayiania, M. Smith, A.J.R. Hensley, L. Scudiero, J.S. McEwen, M. Garcia-Perez, Deconvoluting the XPS spectra for nitrogen-doped chars: An analysis from first principles, Carbon N. Y. 162 (2020) 528–544, https://doi.org/10.1016/j.carbon.2020.02.065.
[53] A.C. Ferrari, J.C. Meyer, V. Scardaci, C. Casiraghi, M. Lazzeri, F. Mauri, S. Piscanec, D. Jiang, K.S. Novoselov, S. Roth, A.K. Geim, Raman Spectrum of Graphene and Graphene Layers, Phys. Rev. Lett. 97 (2006), 187401, https://doi.org/10.1103/PhysRevLett.97.187401.
[54] J.-B. Wu, M.-L. Lin, X. Cong, H.-N. Liu, P.-H. Tan, Raman spectroscopy of graphene-based materials and its applications in related devices, Chem. Soc. Rev. 47 (5) (2018) 1822–1873, https://doi.org/10.1039/C6CS00915H.
[55] C. Maddi, F. Bourquard, V. Barnier, J. Avila, M.C. Asensio, T. Tite, C. Donnet, F. Garrelie, Nano-Architecture of nitrogen-doped graphene films synthesized from a solid CN source, Sci. Rep. 8 (2018) 1–13, https://doi.org/10.1038/s41598-018-21639-9.
[56] R. Beams, L. Gustavo Cançado, L. Novotny, Raman characterization of defects and dopants in graphene, J. Phys. Condens. Matter. 27 (8) (2015) 083002, https://doi.org/10.1088/0953-8984/27/8/083002.
[57] Y. Liu, Q. Li, X.u. Guo, X. Kong, J. Ke, M. Chi, Q. Li, Z. Geng, J. Zeng, A Highly Efficient Metal-Free Electrocatalyst of F-Doped Porous Carbon toward N2 Electroreduction, Adv. Mater. 32 (24) (2020) 1907690, https://doi.org/10.1002/adma.201907690.
[58] J.O. Sofo, A.M. Suarez, G. Usaj, P.S. Cornaglia, A.D. Hernández-Nieves, C. A. Balseiro, Electrical control of the chemical bonding of fluorine on graphene, Phys. Rev. B - Condens. Matter Mater. Phys. 83 (2011) 1–4, https://doi.org/10.1103/PhysRevB.83.081411.
[59] Y. Duan, C.D. Stinespring, B. Chorpening, Electronic StructuresBonding Configurations, and Band-Gap-Opening Properties of Graphene Binding with Low-Concentration Fluorine, ChemistryOpen 4 (5) (2015) 642–650, https://doi.org/10.1002/open.v4.510.1002/open.201500074.
[60] Y. Kim, K.-H. Nam, Y.C. Jung, H. Han, Interfacial adhesion and self-healing kinetics of multi-stimuli responsive colorless polymer bilayers, Compos. Part B Eng. 203 (2020), 108451, https://doi.org/10.1016/j.compositesb.2020.108451.
[61] T. Huhtamäki, X. Tian, J.T. Korhonen, R.H.A. Ras, Surface-wetting characterization using contact-angle measurements, Nat. Protoc. 13 (7) (2018) 1521–1538, https://doi.org/10.1038/s41596-018-0003-z.
[62] J.Y. Chung, J.P. Youngblood, C.M. Stafford, Anisotropic wetting on tunable micro-wrinkled surfaces, Soft Matter. 3 (2007) 1163–1169, https://doi.org/10.1039/b705112c.
[63] R.N. Wenzel, Resistance of solid surfaces to wetting by water, Ind. Eng. Chem. 28 (8) (1936) 988–994, https://doi.org/10.1021/ie50320a024.
[64] L. Gao, T.J. McCarthy, The “lotus effect” explained: Two reasons why two length scales of topography are important, Langmuir. 22 (2006) 2966–2967, https://doi.org/10.1021/la0532149.
[65] R.E. Johnson, R.H. Dettre, Contact angle hysteresis. III. Study of an idealized heterogeneous surface, J. Phys. Chem. 68 (7) (1964) 1744–1750, https://doi.org/10.1021/j100789a012.
[66] S. Zhang, J. Huang, Y. Tang, S. Li, M. Ge, Z. Chen, K. Zhang, Y. Lai, Understanding the Role of Dynamic Wettability for Condensate Microdrop Self-Propelling Based on Designed Superhydrophobic TiO2 Nanostructures, Small. 13 (4) (2017) 1600687, https://doi.org/10.1002/smll.201600687.
[67] A.K. Kota, Y. Li, J.M. Mabry, A. Tuteja, Hierarchically structured superoleophobic surfaces with ultralow contact angle hysteresis, Adv. Mater. 24 (43) (2012) 5838–5843, https://doi.org/10.1002/adma.201202554.
[68] Z.G. Guo, W.M. Liu, Sticky superhydrophobic surface, Appl. Phys. Lett. 90 (2007) 1–3, https://doi.org/10.1063/1.2745251.
[69] J. Xi, L. Jiang, Biomimic superhydrophobic surface with high adhesive forces, Ind. Eng. Chem. Res. 47 (17) (2008) 6354–6357, https://doi.org/10.1021/ie071603n.
[70] S. Wang, L. Jiang, Definition of superhydrophobic states, Adv. Mater. 19 (21) (2007) 3423–3424, https://doi.org/10.1002/adma.v19:2110.1002/adma.200700934.
[71] J. Bico, U. Thiele, D. Quéré, Wetting of textured surfaces, Colloids Surfaces A Physicochem. Eng. Asp. 206 (1-3) (2002) 41–46, https://doi.org/10.1016/S0927-7757(02)00061-4.
[72] L. Feng, Y. Zhang, J. Xi, Y. Zhu, N. Wang, F. Xia, L. Jiang, Petal effect: A superhydrophobic state with high adhesive force, Langmuir. 24 (2008) 4114–4119, https://doi.org/10.1021/la703821h.
[73] A. Al-Azawi, M. Latikka, V. Jokinen, S. Franssila, R.H.A. Ras, Friction and Wetting Transitions of Magnetic Droplets on Micropillared Superhydrophobic Surfaces, Small 13 (2017) 1–7, https://doi.org/10.1002/smll.201700860.
[74] D. Wu, S.-Z. Wu, Q.-D. Chen, Y.-L. Zhang, J. Yao, X.i. Yao, L.-G. Niu, J.-N. Wang, L. Jiang, H.-B. Sun, Curvature-driven reversible in situ switching between pinned and roll-down superhydrophobic states for water droplet transportation, Adv. Mater. 23 (4) (2011) 545–549, https://doi.org/10.1002/adma.v23.410.1002/adma.201001688.
[75] A.B.D. Cassie, S. Baxter, Wettability of porous surfaces, Trans. Faraday Soc. 40 (1944) 546–551.
[76] G. Ding, W. Jiao, L. Chen, M. Yan, L. Hao, R. Wang, A self-sensing, superhydrophobic, heterogeneous graphene network with controllable adhesion behavior, J. Mater. Chem. A. 6 (35) (2018) 16992–17000, https://doi.org/10.1039/C8TA06303F.
[77] C.J. Wu, Y.F. Li, W.Y. Woon, Y.J. Sheng, H.K. Tsao, Contact Angle Hysteresis on Graphene Surfaces and Hysteresis-free Behavior on Oil-infused Graphite Surfaces, Appl. Surf. Sci. 385 (2016) 153–161, https://doi.org/10.1016/j.apsusc.2016.05.059.
[78] H. Zhao, S.J. Park, B.R. Solomon, S. Kim, D. Soto, A.T. Paxson, K.K. Varanasi, A. J. Hart, Synthetic Butterfly Scale Surfaces with Compliance-Tailored Anisotropic Drop Adhesion, Adv. Mater. 31 (14) (2019) 1807686, https://doi.org/10.1002/adma.v31.1410.1002/adma.201807686.
[79] Y. Wang, Y. Wang, P. Zhang, F.u. Liu, S. Luo, Laser-Induced Freestanding Graphene Papers: A New Route of Scalable Fabrication with Tunable Morphologies and Properties for Multifunctional Devices and Structures, Small. 14 (36) (2018) 1802350, https://doi.org/10.1002/smll.201802350.